How to cite: *Angew. Chem. Int. Ed.* **2025**, *64*, e202417429
doi.org/10.1002/anie.202417429

Porphyrins

High Charge Carrier Mobility in Porphyrin Nanoribbons

He Zhu, Guanzhao Wen, Wenhao Zheng, Nicholas H. Rees, Wojciech Stawski, Hai I. Wang, Mischa Bonn, and Harry L. Anderson**

Abstract: Polydisperse edge-fused nickel(II) porphyrin nanoribbons have been synthesized by Yamamoto coupling followed by gold(III)-mediated fusion, with average degrees of polymerization of up to 37 repeat units (length 31 nm). Time-resolved optical-pump terahertz spectroscopy measurements indicate that photogenerated charge carriers have dc mobilities of up to 205 $cm^2 V^{-1} s^{-1}$ in these nanoribbons, exceeding the values previously reported for most other types of nanoribbon or π-conjugated polymer.

Charge carrier mobility is a key performance metric for organic semiconductors, particularly for applications in field-effect transistors.[1] One approach to optimizing the carrier mobility in conjugated polymers is to create rigid ladder-type structures, to prevent torsional disorder and enhance orbital overlap.[2] Graphene nanoribbons (GNRs) benefit from this ladder-type conformational control and multiple π-conjugation pathways, which probably contribute to their excellent charge carrier mobilities.[3] Recently, there have been several studies of charge mobility in other types of π-conjugated nanoribbons, not derived from the graphene hexagonal lattice.[4,5] Here, we present the synthesis of a polydisperse nanoribbon consisting of edge-fused Ni(II) porphyrins ***f*-PN** (Scheme 1), with an average degree of polymerization of up to 37 porphyrin repeat units and an extremely low band gap of 0.47 eV. Time-resolved optical-pump THz-probe spectroscopy experiments[6] show that these materials have charge mobilities of up to about 200 $cm^2 V^{-1} s^{-1}$, higher than most values reported for GNRs, measured by the same technique.[3]

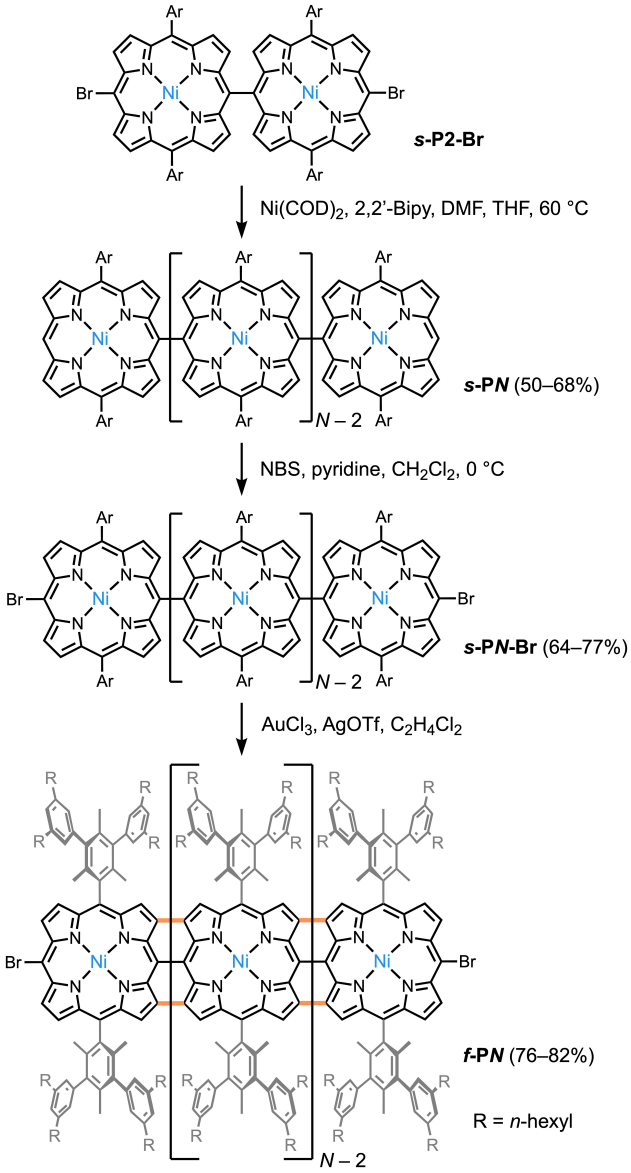

Scheme 1. Synthesis of ***f*-PN**. (COD is 1,5-cyclooctadiene. Ar is a bulky aryl solubilizing group as shown in full for ***f*-PN**.)

Edge-fused porphyrin oligomers of the general type ***f*-PN** (also known as 'porphyrin tapes') were first synthesized by Osuka and co-workers.[7] These nanoribbons exhibit remarkably small HOMO–LUMO gaps. Polarons in these nanoribbons are highly delocalized, covering more than ten porphyrin units (>8.5 nm).[8] Single-molecule charge-transport experiments demonstrate that these nanoribbons exhib-

[*] Dr. H. Zhu, Dr. N. H. Rees, Dr. W. Stawski, Prof. Dr. H. L. Anderson
Department of Chemistry
University of Oxford
Chemistry Research Laboratory, Oxford OX1 3TA, UK
E-mail: harry.anderson@chem.ox.ac.uk
G. Wen, Dr. W. Zheng, Prof. H. I. Wang, Prof. M. Bonn
Department of Molecular Spectroscopy
Max Planck Institute for Polymer Research
Ackermannweg 10, 55128 Mainz, Germany
E-mail: bonn@mpip-mainz.mpg.de

© 2024 The Author(s). Angewandte Chemie International Edition published by Wiley-VCH GmbH. This is an open access article under the terms of the Creative Commons Attribution License, which permits use, distribution and reproduction in any medium, provided the original work is properly cited.

© 2024 The Author(s). Angewandte Chemie International Edition published by Wiley-VCH GmbH

it phase-coherent ballistic transport, with molecular conductances almost independent of length.[9,10] All these features suggest that porphyrin nanoribbons are likely to have high charge-carrier mobilities.

Previously, monodisperse porphyrin nanoribbons consisting of up to 24 porphyrin units have been synthesized.[7c] In this study, we chose to prepare polydisperse nanoribbons, so as to access long chains directly from readily available precursors. We decided to work with Ni(II) porphyrins because Ni-porphyrin nanoribbons are more stable and less easily oxidized than the corresponding Zn complexes.[9,10] Bulky 3,5-diaryl mesityl solubilizing groups (Scheme 1) were used to enhance solubility and hinder aggregation. The methyl substituents *ortho* to the porphyrin prevent accidental fusion of the aryl group to the porphyrin (5-membered ring formation), during the final step in synthesizing ***f*-P*N***.[5,11–13]

Yamamoto coupling of the singly-linked dibromo porphyrin dimer ***s*-P2-Br**, with bis(cyclooctadiene)nickel(0) and 2,2'-bipyridyl in DMF/THF was used to prepare polymer ***s*-P*N***. The molecular weight distribution from this reaction showed batch-to-batch variation (probably due to accidental traces of O_2 or water in the reaction mixture). In this study, we compared three batches designated ***s*-P*N*(1)**, ***s*-P*N*(2)** and ***s*-P*N*(3)**. The gel-permeation chromatography (GPC) trace of the crude reaction mixture for ***s*-P*N*(3)** is compared with traces for all three batches, after removal of short oligomers by preparative GPC, in Figure 1a. The number-average molecular weights (M_n) and degrees of polymerization ($\bar{N}_n$), measured by GPC relative to polystyrene standards, are listed in Table 1. There is excellent agreement between these degrees of polymerization and the range of oligomers observed by MALDI-TOF mass spectrometry, as illustrated for ***s*-P*N*(3)** in Figure 1b, and by the data listed in Table 1 ($\bar{N}_n$ vs. $N_{MALDI,\,peak}$; see also Figure S5).

The NMR and mass spectra of ***s*-P*N*** showed that the terminal *meso*-positions bear hydrogen atoms, not bromine, due to reductive debromination during Yamamoto coupling (Figure S20). The next step was to brominate these positions, to prevent accidental *meso-meso* coupling during the formation of the ***f*-P*N*** nanoribbon. Treatment of ***s*-P*N*** with *N*-bromosuccinimide gave ***s*-P*N*-Br** in high yield (Scheme 1). Oxidative fusion and planarization of ***s*-P*N*-Br** to ***f*-P*N*** was achieved using $AuCl_3$/AgOTf.[9a,14] The reaction was monitored by UV–vis–NIR spectroscopy, and oxidation was continued until there was no further change in the absorption spectrum (Figure S36). Essentially identical spectral changes were observed when ***s*-P*N*-Br** was oxidized with DDQ/TfOH,[5,13] indicating that both reaction conditions give full conversion to ***f*-P*N***, but we prefer the $AuCl_3$/AgOTf conditions because they allow easier purification of the product. Three batches of the nanoribbon, designated ***f*-P*N*(1)**, ***f*-P*N*(2)** and ***f*-P*N*(3)**, were synthesized from ***s*-P*N*(1)**, ***s*-P*N*(2)** and ***s*-P*N*(3)**. The vis-NIR spectra of these three batches (recorded as thin films on a CaF_2 plate, Figure 2) are very similar, but a slight red-shift in the NIR absorption is observed with increasing chain length, as expected, with absorption maxima at 2178, 2222 and 2276 nm, respectively.[15] These absorption wavelengths are consistent with those previously reported for nickel porphyrin nanoribbons,[9a] which are blue-shifted relative to zinc porphyrin nanoribbons.[9a,10] The optical band gap of ***f*-P*N***, estimated from the onset of the absorption band, is 0.47 eV (within error, the same for all three batches).

The singly-linked porphyrin polymer ***s*-P*N*** is soluble in organic solvents. While the ***f*-P*N*** nanoribbon is sufficiently

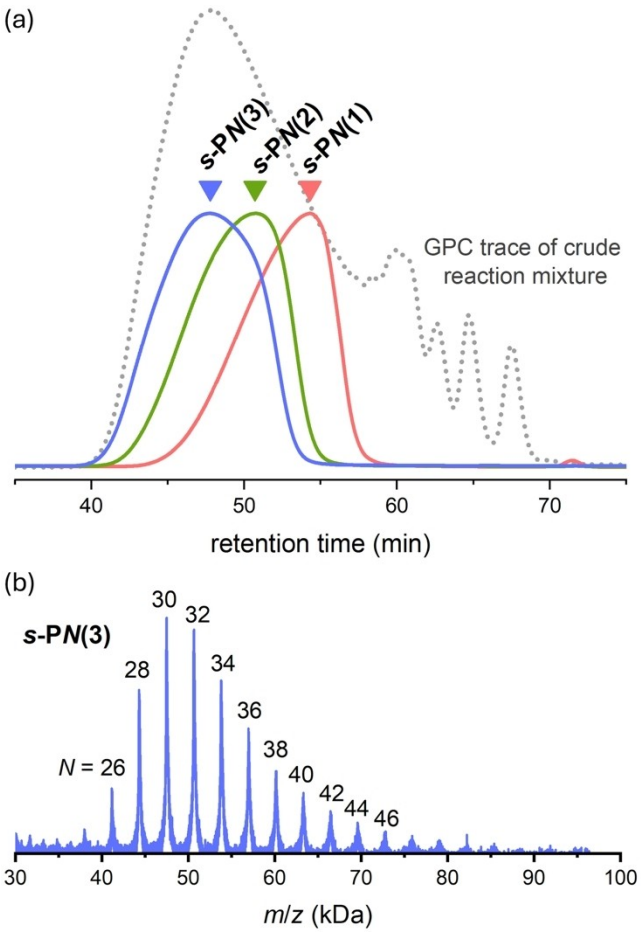

Figure 1. (a) GPC traces of three individual batches of ***f*-P*N***: ***s*-P*N*(1)** (red), ***s*-P*N*(2)** (green) and ***s*-P*N*(3)** (blue) and a trace of the crude reaction mixture (gray dashed) for ***s*-P*N*(3)**; (b) MALDI-TOF mass spectrum of ***s*-P*N*(3)** measured with *trans*-2-[3-(4-*tert*-butylphenyl)-2-methyl-2-propenylidene]malononitrile (DCTB) as the matrix, in the linear mode.

Table 1: Molecular weight distributions of three batches of ***s*-P*N***.[a]

batch	M_n (kDa)	$Đ$	$\bar{N}_n$	$N_{MALDI,\,peak}$
***s*-P*N*(1)**	23.8	1.08	15	18
***s*-P*N*(2)**	42.2	1.21	27	26
***s*-P*N*(3)**	57.7	1.39	37	30

[a] M_n is the number-average molecular weight, determined by GPC in chlorobenzene, relative to polystyrene standards; $Đ$ is the polydispersity, M_w/M_n. $\bar{N}_n$ is the number-average degree of polymerization from GPC; $N_{MALDI,\,peak}$ is the most abundant chain length observed by MALDI-TOF mass spectrometry.

© 2024 The Author(s). Angewandte Chemie International Edition published by Wiley-VCH GmbH

15213773, 2025, 6, Downloaded from https://onlinelibrary.wiley.com/doi/10.1002/anie.202417429 by NICE, National Institute for Health and Care Excellence, Wiley Online Library on [22/05/2026]. See the Terms and Conditions (https://onlinelibrary.wiley.com/terms-and-conditions) on Wiley Online Library for rules of use; OA articles are governed by the applicable Creative Commons License

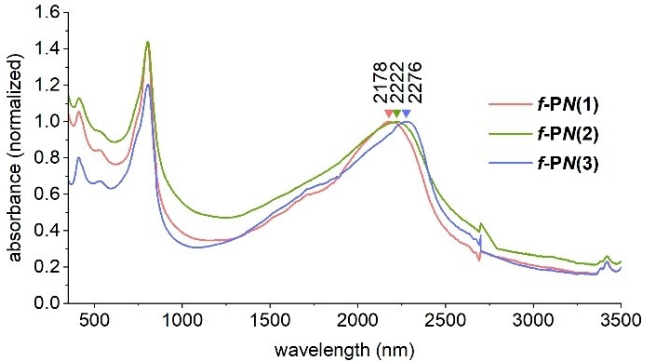

Figure 2. Visible–NIR absorbance spectra of three batches of Ni(II) porphyrin nanoribbons: ***f*-PN(1)** (red), ***f*-PN(2)** (green) and ***f*-PN(3)** (blue), recorded on thin films.[15]

soluble for recording solution-phase UV/Vis-NIR spectra, it is not soluble enough for solution-phase NMR spectroscopy. Therefore, we compared the solid-state NMR spectra of ***s*-PN-Br** and ***f*-PN**. The solid-state magic-angle spinning (MAS) ^{1}H NMR spectra of ***s*-PN-Br** and ***f*-PN** exhibit broad peaks in the aromatic region, and the shoulder assigned to β-protons diminishes on conversion of ***s*-PN-Br** to ***f*-PN** (Figure S21), indicating removal of these hydrogen atoms. Comparison of the cross polarization non-quaternary suppression (CP-NQS) ^{13}C NMR spectra of ***s*-PN-Br** and ***f*-PN** shows the formation of new quaternary carbon environments in ***f*-PN**, consistent with successful fusion and dehydrogenation (Figure S23).

Ultrafast optical-pump THz-probe spectroscopy is a powerful technique to measure the intra-chain mobility of photo-generated charge carriers, without requiring electrical contacts.[6] Here, we used this technique to study the charge carrier mobility in three batches of ***f*-PN**, as thin films on silica. Free charge carriers were generated using an optical pulse (400 nm, 100 fs duration). The transient photoconductivity ($\Delta\sigma$) was probed by a single-cycle THz pulse (with a bandwidth of ~2 THz). The real part of THz conductivity is proportional to the attenuation of transmitted THz electric-field by free charge carriers. In contrast, excitons, bound electron-hole pairs, merely cause a phase shift of the waveform through the imaginary component of the conductivity (i.e., the induced polarizability).[3] The photoconductivity dynamics (Figure 3a) show a sub-picosecond rise in the time-resolved complex photoconductivity, due to the generation of free carriers. The signal then decays due to exciton formation, evidenced by a relative increase in imaginary conductivity.[3–5] Figure 3a shows that photoconductivity increases with the ribbon length, implying that longitudinal confinement affects THz conductivity.

The frequency-resolved complex photoconductivities for each sample, recorded at 1.5 ps after the maximum THz photoconductivity, are plotted in Figure 3b. These curves are well described by the Drude–Smith model, following Equation (1):

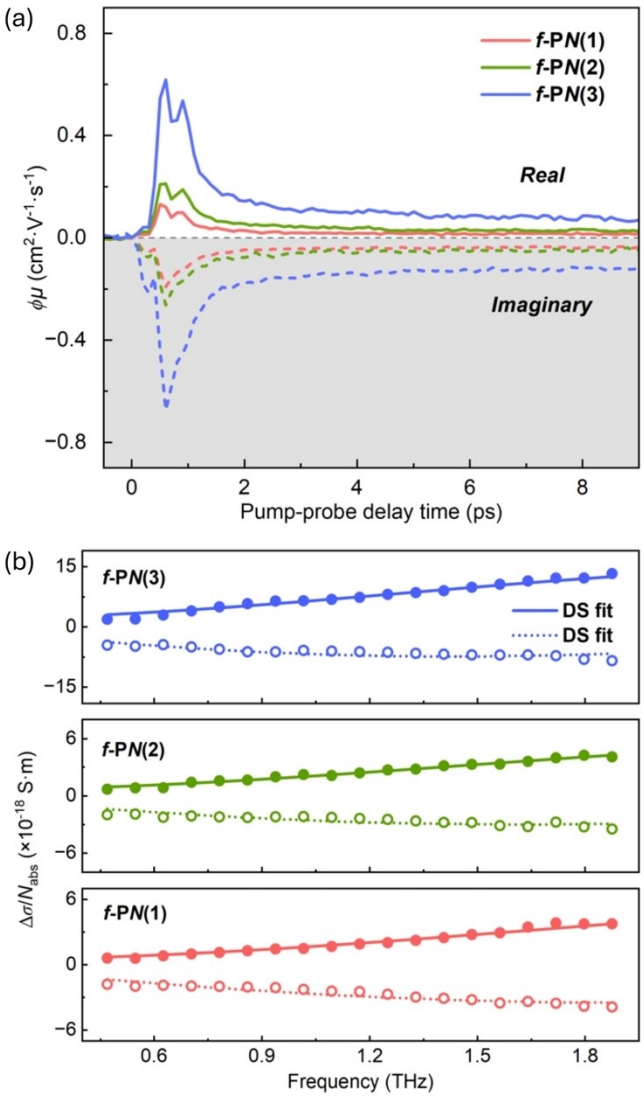

Figure 3. (a) Time-resolved complex photoconductivity measured for thin films of ***f*-PN(1)**, ***f*-PN(2)** and ***f*-PN(3)**. (b) Frequency-resolved THz photoconductivity of ***f*-PN(1)**, ***f*-PN(2)** and ***f*-PN(3)** measured at $t_p \approx 1.5$ ps after the maximum THz photoconductivity. The data are fitted by the Drude–Smith model.

$$\sigma_{DS} = \frac{\varepsilon_0 \omega_p^2 \tau_{DS}}{1 - i\omega\tau_{DS}} \left(1 + \frac{c}{1 - i\omega_p \tau_{DS}}\right) \quad (1)$$

where ε_0 is the vacuum permittivity, ω_p is the plasma oscillation resonance of charge carriers, and τ_{DS} is the averaged carrier momentum scattering time. The parameter c ($-1 \le c \le 0$) describes the spatial confinement experienced by charge carriers, limiting long-range dc transport. The obtained absolute values of c decrease with increasing ribbon length (in the range -0.97 to -0.93) for all batches of ***f*-PN** (Table 2), indicating a reduced spatial confinement for charge transport in long ribbons. The scattering times for all three batches lie in the range 30–46 fs, which is in the range previously reported for GNRs (see the overview of high-mobility nanoribbons in SI, Table S2).[3] The values of

© 2024 The Author(s). Angewandte Chemie International Edition published by Wiley-VCH GmbH

15213773, 2025, 6, Downloaded from https://onlinelibrary.wiley.com/doi/10.1002/anie.202417429 by NICE, National Institute for Health and Care Excellence, Wiley Online Library on [22/05/2026]. See the Terms and Conditions (https://onlinelibrary.wiley.com/terms-and-conditions) on Wiley Online Library for rules of use; OA articles are governed by the applicable Creative Commons License

Table 2: THz photoconductivity data for nanoribbon ***f*-PN** determined by fitting the data to the Drude–Smith model.[a]

batch	average chain length (nm)[b]	c	τ_{DS} (fs)	μ_{dc} ($cm^2V^{-1}s^{-1}$)
***f*-PN(1)**	13	-0.97 ± 0.01	33 ± 3	64 ± 22
***f*-PN(2)**	22	-0.95 ± 0.01	39 ± 2	127 ± 26
***f*-PN(3)**	31	-0.93 ± 0.01	45 ± 1	205 ± 30

[a] c is the localization parameter; τ_{DS} is the carrier scattering time; μ_{dc} is the intrinsic carrier mobility in the dc limit, calculated from Equation (2). [b] The chain length is estimated by multiplying the calculated length of a repeat unit (0.84 nm) by the average degree of polymerization ($\bar{N}_n$) from Table 1.

τ_{DS} and c can be used to estimate the mobility for each sample in the dc-limit, μ_{dc}, using Equation (2):[6]

$$\mu_{dc} = \frac{e\tau_{DS}}{m^*}(1+c) \quad (2)$$

where e is the elementary charge and m^* is the effective mass, which has previously been estimated from band structure calculations on nickel(II) porphyrin nanoribbons ($0.027\,m_0$, where m_0 is the mass of an electron).[5,16] Values of μ_{dc} are in the range 64–205 $cm^2V^{-1}s^{-1}$ for ***f*-PN(1)** to ***f*-PN(3)** (Table 2). The inferred dc carrier mobilities are limited by backscattering effects originating from structural deformations and/or the limited ribbon lengths.[3b] In long and deformation-free ribbons, aligned with the electric field, the intrinsic carrier mobility is expected to approach 3000 $cm^2V^{-1}s^{-1}$ (based on $\tau_{DS}=45$ fs). The intrinsic local carrier mobility of porphyrin nanoribbons is among the highest reported for any solution-synthesized nanoribbon characterized by terahertz spectroscopy (Table S2).[3c,5,17] Comparison of the scattering time and band structure of the nickel(II) porphyrin nanoribbon with those of solution-synthesized GNRs, shows that the high intrinsic carrier mobility of ***f*-PN** can be attributed to its strong band dispersion, which results in a small effective mass. The extremely high intrinsic mobility of the nickel(II) porphyrin nanoribbon is in line with a recent GNR field-effect device in which a mobility over 1000 $cm^2V^{-1}s^{-1}$ was reported.[18] Previously, we investigated the hole mobility in butadiyne-linked porphyrin polymers, as non-covalent ladder complexes, using time-resolved microwave conductivity.[2c] The much lower mobility inferred from those experiments (0.93 $cm^2V^{-1}s^{-1}$) compared with that for ***f*-PN** from THz spectroscopy, probably reflects the different technique as well as the weaker electronic coupling in butadiyne-linked porphyrin polymers.[9b]

In conclusion, this work has demonstrated the synthesis of porphyrin polymers with a high degree of polymerization ($\bar{N}=37$; number-average length 31 nm) through Yamamoto coupling. Oxidative fusion gives the porphyrin nanoribbon ***f*-PN**, which was characterized by solid-state NMR and UV–vis–NIR absorption spectroscopy (band gap 0.47 eV). Optical-pump THz-probe experiments show that charge carriers are exceptionally mobile. Three batches of the nanoribbon with different average chain lengths were compared, revealing that the mobility increases dramatically with increasing chain length. This strong length-dependence emphasizes that the longitudinal confinement in porphyrin nanoribbons limits the THz conductivity. The highest charge carrier mobility in these samples reaches 205 $cm^2V^{-1}s^{-1}$, in dc-limit.[16] These results reveal that porphyrin nanoribbons have higher charge mobilities than most solution-synthesized GNRs, highlighting the potential applications of these materials in molecular electronics.

Supporting Information

The authors have cited additional references within the Supporting Information.[19–21]

Acknowledgements

We thank the European Research Council (grant 885606, ARO-MAT) for support. G.W. acknowledges the fellowship support from the China Scholarship Council (CSC). For the purpose of Open Access, the authors have applied a CC BY public copyright license to any Author Accepted Manuscript (AAM) version arising from this publication.

Conflict of Interest

The authors declare no conflict of interest.

Data Availability Statement

The data that support the findings of this study are available in the supplementary material of this article.

Keywords: porphyrins · polymers · high charge carrier mobility · small band gap · time-resolved spectroscopy

[1] S. Fratini, M. Nikolka, A. Salleo, G. Schweicher, H. Sirringhaus, *Nat. Mater.* **2020**, *19*, 491–502.

[2] a) A. Babel, S. A. Jenekhe, *J. Am. Chem. Soc.* **2003**, *125*, 13656–136576; b) P. Prins, F. C. Grozema, J. M. Schins, S. Patil, U. Scherf, L. D. A. Siebbeles, *Phys. Rev. Lett.* **2006**, *96*, 146601; c) F. C. Grozema, C. Houarner-Rassin, P. Prins, L. D. A. Siebbeles, H. L. Anderson, *J. Am. Chem. Soc.* **2007**, *129*, 13370–13371.

[3] a) S. A. Jensen, R. Ulbricht, A. Narita, X. Feng, K. Müllen, T. Hertel, D. Turchinovich, M. Bonn, *Nano Lett.* **2013**, *13*, 5925–5930; b) I. Ivanov, Y. Hu, S. Osella, U. Beser, H. I. Wang, D. Beljonne, A. Narita, K. Müllen, D. Turchinovich, M. Bonn, *J. Am. Chem. Soc.* **2017**, *139*, 7982–7988; c) X. Wang, J. Ma, W. Zheng, S. Osella, N. Arisnabarreta, J. Droste, Gianluca Serra, O. Ivasenko, A. Lucotti, D. Beljonne, M. Bonn, X. Liu, M. R. Hansen, M. Tommasini, S. De Feyter, J. Liu, H. I. Wang, X. Feng, *J. Am. Chem. Soc.* **2022**, *144*, 228–235; d) X. Yao, H. Zhang, F. Kong, A. Hinaut, R. Pawlak, M. Okuno, R. Graf, P. N. Horton, S. J. Coles, E. Meyer, L. Bogani, M. Bonn, H. I.

© 2024 The Author(s). Angewandte Chemie International Edition published by Wiley-VCH GmbH

15213773, 2025, 6, Downloaded from https://onlinelibrary.wiley.com/doi/10.1002/anie.202417429 by NICE, National Institute for Health and Care Excellence, Wiley Online Library on [22/05/2026]. See the Terms and Conditions (https://onlinelibrary.wiley.com/terms-and-conditions) on Wiley Online Library for rules of use; OA articles are governed by the applicable Creative Commons License

Wang, K. Müllen, A. Narita, *Angew. Chem. Int. Ed.* **2023**, *62*, e202312610.
[4] a) R. K. Dubey, M. Marongiu, S. Fu, G. Wen, M. Bonn, H. I. Wang, M. Melle-Franco, A. Mateo-Alonso, *Chem* **2023**, *9*, 2983–2996; b) L. Zhao, Z. Wu, H. Qin, G. Bin, J. Gao, W. Zeng, Y. Zhao, H. Chen, *Chem. Sci.* **2024**, *15*, 11594–11603.
[5] Q. Chen, A. Lodi, H. Zhang, A. Gee, H. I. Wang, F. Kong, M. Clarke, M. Edmondson, J. Hart, J. N. O'Shea, W. Stawski, J. Baugh, A. Narita, A. Saywell, M. Bonn, K. Müllen, L. Bogani, H. L. Anderson, *Nat. Chem.* **2024**, *16*, 1133–1140.
[6] a) E. Ulbricht, E. Hendry, J. Shan, T. F. Heiz, M. Bonn, *Rev. Mod. Phys.* **2011**, *83*, 543–586; b) P. Kužel, H. Nemec, *Adv. Opt. Mater.* **2020**, *8*, 1900623.
[7] a) A. Tsuda, A. Osuka, *Science* **2001**, *293*, 79–82; b) T. Ikeda, J. M. Lintuluoto, N. Aratani, Z. S. Yoon, D. Kim, A. Osuka, *Eur. J. Org. Chem.* **2006**, 3193–3204; c) T. Ikeda, N. Aratani, A. Osuka, *Chem. Asian J.* **2009**, *4*, 1248–1256.
[8] S. M. Kopp, J.-R. Deng, A. J. Redman, H. Gotfredsen, R. M. J. Jacobs, H. L. Anderson, C. R. Timmel, *Chem* **2024**, DOI: 10.1016/j.chempr.2024.07.011.
[9] a) J.-R. Deng, M. T. González, H. Zhu, H. L. Anderson, E. Leary, *J. Am. Chem. Soc.* **2024**, *146*, 3651–3659; b) E. Leary, B. Limburg, A. Alanazy, S. Sangtarash, I. Grace, K. Swada, L. J. Esdaile, M. Noori, M. T. González, G. Rubio-Bollinger, H. Sadeghi, A. Hodgson, N. Agraït, S. J. Higgins, C. J. Lambert, H. L. Anderson, R. J. Nichols, *J. Am. Chem. Soc.* **2018**, *140*, 12877–12883.
[10] Z. Chen, J.-R. Deng, S. Hou, X. Bian, J. L. Swett, Q. Wu, J. Baugh, G. A. D. Briggs, J. A. Mol, C. J. Lambert, H. L. Anderson, J. O. Thomas, *J. Am. Chem. Soc.* **2023**, *145*, 15265–15274.
[11] Q. Chen, L. Brambilla, L. Daukiya, K. S. Mali, S. De Feyter, M. Tommasini, K. Müllen, A. Narita, *Angew. Chem. Int. Ed.* **2018**, *57*, 11233–11237.
[12] M. M. Martin, C. Oleszak, F. Hampel, N. Jux, *Eur. J. Org. Chem.* **2020**, 6758–6762.
[13] H. Zhu, Q. Chen, I. Rončević, K. E. Christensen, H. L. Anderson, *Angew. Chem. Int. Ed.* **2023**, *62*, e202307035.
[14] A. K. Sahoo, Y. Nakamura, N. Aratani, K. S. Kim, S. B. Noh, H. Shinokubo, D. Kim, A. Osuka, *Org. Lett.* **2006**, *8*, 4141–4144.
[15] Figure shows visible-NIR spectra of thin films of ***f*-P*N*** on CaF_2. Similar spectra were also recorded for solutions of ***f*-P*N*** in toluene, but they are interrupted by overlapping vibrational bands from the solvent, see Figure S38.
[16] The value of the effective mass $m^* = 0.027\ m_0$ was calculated in reference [5]. A value of $m^* = 0.020\ m_0$ was calculated for the same nickel(II) ***f*-P*N*** nanoribbon in reference [13]. Taking the smaller value of m^* would increase our estimate of μ_{dc} by 35 %.
[17] a) Z. Chen, H. I. Wang, J. Teyssandier, K. S. Mali, T. Dumslaff, I. Ivanov, W. Zhang, P. Ruffieux, R. Fasel, H. J. Räder, D. Turchinovich, S. De Feyter, X. Feng, M. Kläui, A. Narita, M. Bonn, K. Müllen, *J. Am. Chem. Soc.* **2017**, *139*, 3635–3638; b) W. Niu, J. Ma, P. Soltani, W. Zheng, F. Liu, A. A. Popov, J. J. Weigand, H. Komber, E. Poliani, C. Casiraghi, J. Droste, M. Ryan Hansen, S. Osella, D. Beljonne, M. Bonn, H. I. Wang, X. Feng, J. Liu, Y. Mai, *J. Am. Chem. Soc.* **2020**, *142*, 18293–18298; c) K. Liu, W. Zheng, S. Osella, Z.-L. Qiu, S. Böckmann, W. Niu, L. Meingast, H. Komber, S. Obermann, R. Gillen, M. Bonn, M. R. Hansen, J. Maultzsch, H. I. Wang, J. Ma, X. Feng, *J. Am. Chem. Soc.* **2024**, *146*, 1026–1034.
[18] B. Lyu, J. Chen, S. Wang, S. Lou, P. Shen, J. Xie, L. Qiu, I. Mitchell, C. Li, C. Hu, X. Zhou, K. Watanabe, T. Taniguchi, X. Wang, J. Jia, Q. Liang, G. Chen, T. Li, S. Wang, W. Ouyang, O. Hod, F. Ding, M. Urbakh, Z. Shi, *Nature* **2024**, *628*, 758–764.
[19] G. M. Sheldrick, SHELXT – Integrated space-group and crystal-structure determination. *Acta Crystallogr.* **2015**, *A71*, 3–8.
[20] G. M. Sheldrick, Crystal structure refinement with SHELXL. *Acta Crystallogr.* **2015**, *C71*, 3–8.
[21] O. V. Dolomanov, L. J. Bourhis, R. J. Gildea, J. A. K. Howard, H. Puschmann, OLEX2: A complete structure solution, refinement and analysis program. *J. Appl. Crystallogr.* **2009**, *42*, 339–341.

Manuscript received: September 10, 2024
Accepted manuscript online: November 12, 2024
Version of record online: November 28, 2024

© 2024 The Author(s). Angewandte Chemie International Edition published by Wiley-VCH GmbH

15213773, 2025, 6, Downloaded from https://onlinelibrary.wiley.com/doi/10.1002/anie.202417429 by NICE, National Institute for Health and Care Excellence, Wiley Online Library on [22/05/2026]. See the Terms and Conditions (https://onlinelibrary.wiley.com/terms-and-conditions) on Wiley Online Library for rules of use; OA articles are governed by the applicable Creative Commons License